Int. J. Electrochem. Sci., 15 **(2020)** 10173 – 10183, doi: 10.20964/2020.10.77

International Journal of
ELECTROCHEMICAL
SCIENCE
www.electrochemsci.org

A Sheet-like SnO_2@SiO_2/graphite Composite as Anode Material with Excellent Performance for Lithium-Ion Batteries

Jin Ke, Yefeng Feng, Bingwen Yang, Kaidan Wu, Xiaoqian Deng, Miao He[*]

School of Physics and Optoelectronic Engineering, Guangdong University of Technology, Guangzhou 510006, Guangdong, Peoples R China
[*]E-mail: herofate666@126.com

Received: 29 June 2020 / *Accepted:* 16 August 2020 / *Published:* 31 August 2020

SnO_2-based composites are widely used as anode materials for lithium-ion batteries owing to their high theoretical capacities. However, their poor stability limits their practical applications. Therefore, in this study, SnO_2@SiO_2/graphite composite was designed and fabricated using the balling method. SiO_2 effectively buffers the volume expansion of SnO_2 during the lithiation and delithiation processes. Furthermore, the graphite ground into the sheet wrapping the hybrid SnO_2 and SiO_2 nanoparticles improves the volume change tolerance and enhances the electrochemical properties of the materials. As a result, the SnO_2@SiO_2/graphite composite exhibits a high specific capacity and excellent rate performance. In the initial charge/discharge cycle, the capacity of the SnO_2@SiO_2/graphite anode reaches 2489 mA h g^{-1} at a current density of 200 mA g^{-1} and retains a capacity of 1132 mA h g^{-1} after 80 cycles, which is better than that of the SnO_2@graphite composite and SnO_2.

Keywords: SnO_2, graphite nanosheet, anode, lithium-ion battery

1. INTRODUCTION

With the rapid development of portable devices and electric vehicles, lithium-ion batteries (LIBs) have become indispensable because of their high energy density, long cycle life, and low environmental impact compared to fossil fuels and nuclear energy [1-5]. One of the focuses in the development of LIBs is the search for materials with a higher capacity than graphite anodes. Among the metal oxides studied as the anode in LIBs, SnO_2 is one of the most suitable substitutes for graphite because of its high theoretical capacity (1494 mA h g^{-1}) [6]. However, the practical utilisation of SnO_2 in LIBs is limited because of the large volume change during the lithiation/delithiation reaction, which leads to several critical problems, including pulverization of the SnO_2 particles, instability of the electrode, and low initial coulombic efficiency (ICE) [7, 8].

In recent years, many researchers have proposed feasible measures to solve these issues. For example, it has been proven that nanostructures such as nanowire arrays and carbon nanotube papers effectively overcome these problems owing to their good electrical contact with the current collector and great tolerance against volume change [9, 10]. In addition, SnO_2 composites with graphite [11] , graphene [12], and transition metal oxides such as Fe_3O_4, MnO_2, and CuO [13-15], as well as a series of ternary composites comprised SnO_2 [16, 17], have been utilised in this regard.

In this study, we fabricated a SnO_2@SiO_2/graphite composite through simple ball milling with carbon nanosheets coating with SnO_2 and SiO_2 nanoparticles. Through the unique architecture of the composite, the carbon nanosheets not only accommodate the volume change caused by Li^+ insertion or extraction, but also anchor the SnO_2 and SiO_2 nanoparticles to prevent aggregation, thereby enhancing the electronic conductivity. The as-fabricated SnO_2@SiO_2/graphite composite demonstrates a high capacity and good cycling stability.

2. EXPERIMENTAL

2.1. Synthesis of SnO_2 nanoparticles

SnO_2 nanoparticles were fabricated through a facile hydrothermal method. First, 1.3 g of $Na_2SnO_3 \cdot 3H_2O$ and 3 g of urea were added into a solution consisting of 30 mL of deionized water and 30 mL of anhydrous ethanol. Afterwards, the mixture was stirred for 2 h to obtain a uniform solution, and then it was placed into an autoclave at 200 °C for 20 h to produce pure SnO_2 nanoparticles.

2.2. Synthesis of SnO_2@SiO_2/G composite

The powders of SnO_2, SiO (99.9%), and graphite were mixed according to the weight ratio 7:0.5:2.5 through two-step ball milling. The SnO_2 and SiO powders (99.9%) were ground in a ball mill machine to acquire a SnO_2-SiO_2 mixture in air. The SnO_2-SiO_2 mixture was further milled with graphite in the machine at 400 rpm for 5 h to obtain the SnO_2@SiO_2/graphite composite (SnO_2@SiO_2/G). A SnO_2@graphite composite (SnO_2@G) and SnO_2 were also prepared to illustrate the performance of these negative materials under the same conditions. The machine was rested for 30 min after every 60 min of operation to avoid high temperature during ball milling.

2.3. Characterization

The crystal structure of the SnO_2@SiO_2/G was observed using an X-ray diffractometer (XRD, Philips XPert MPD). The morphology and microstructure of the composites were analyzed with a scanning electron microscope (SEM, Zeiss Supra 40) and a transmission electron microscope (TEM, JEOL 2011). Raman spectroscopy (Raman, HORIBA Labram) and X-ray photoelectron spectroscopy (XPS, Escalab 250Xi) were used to identify the composition of the composites and determine their

valence state. Thermogravimetric analysis (TGA, SDRO600) was conducted at a temperature range of 25−650 °C in oxygen at a heating rate of 10 °C min^{-1}.

2.4. Electrochemical measurements

The electrochemical performance of the composites was characterized using coin-type half cells (CR2025). The negative electrode was prepared by dissolving 70 wt% of the active substance, 15 wt% of the conductive carbon, and 15 wt% of the binder in N-methyl-2-pyrrolidone. The resulting mixture was dried in a vacuum oven at 60 ℃ for 24 h and then cut into disk with a diameter of 16 mm. A Li foil was used as the opposite electrode, polyethylene membranes were used as the diaphragm, and $LiPF_6$ was used as the electrolyte. The cycle and rate performances were measured using battery testers (CT2001A, Land). Cyclic voltammetry (CV) and electrochemical impedance spectroscopy (EIS) were performed on an electrochemical workstation (Interface 1000, Gamry).

3. RESULTS AND DISCUSSION

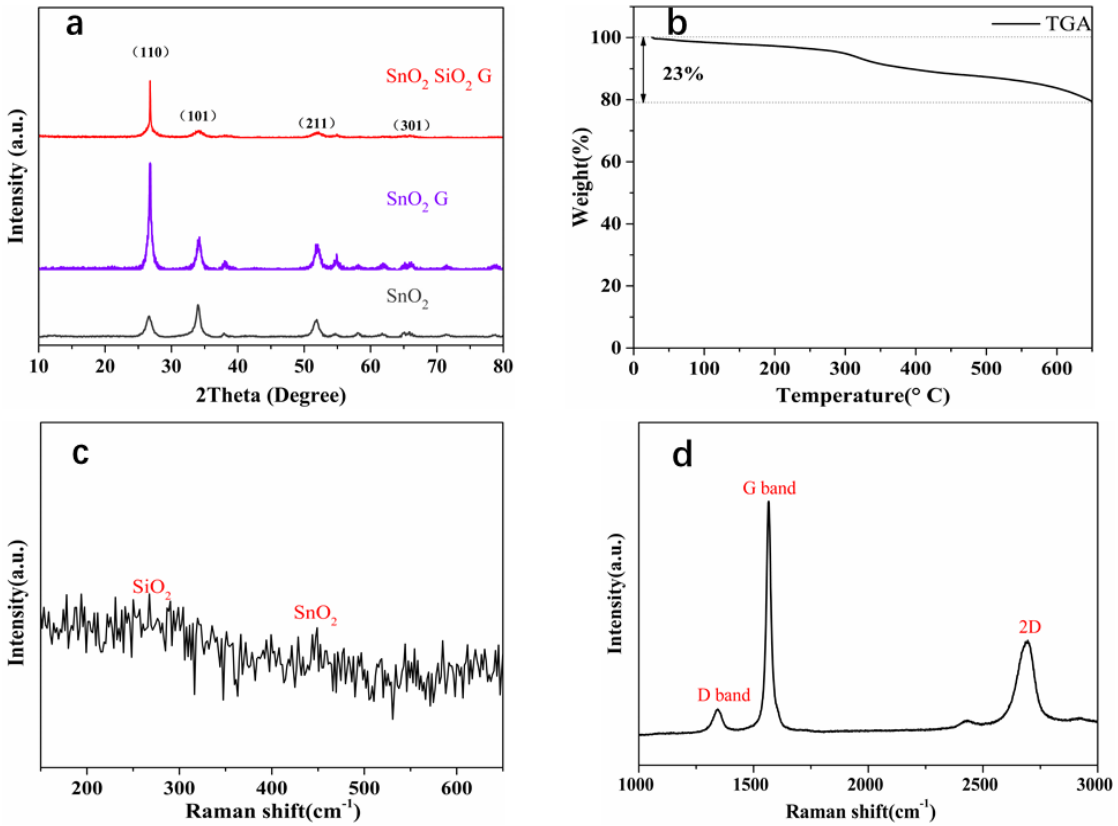

Figure 1. (a) XRD patterns of SnO_2, SnO_2@G, and SnO_2@SiO_2/G. (b) TGA curve of SnO_2@SiO_2/G. (c, d) Raman spectra of SnO2@SiO_2/G.

To investigate the crystal phases of SnO_2, SnO_2@G, and SnO_2@SiO_2/G composites, XRD was carried out, and the results are displayed in Fig. 1(a). Based on the XRD patterns, the (110), (101), (211),

and (301) planes of the crystalline SnO_2 nanoparticles are present, and all the diffraction peaks correspond to the standard tetragonal SnO_2 phase (card No. 72-114) [18, 19]. The XRD pattern of the SnO_2@ SiO_2/G composite shows varying diffraction peaks compared to the pure SnO_2 phase, indicating that the addition of SiO_2 and graphite leads to broader peaks. The diffraction peaks of the (101), (211), and (301) planes in the SnO_2@SiO_2/G composite are weaker than those in the pure SnO_2, suggesting that SnO_2 is embedded in the graphite. TGA was used to determine the carbon content in the composite, and the results are shown in Fig. 1 (b). Visibly, the weight percent of the SnO_2@SiO_2/G composite drops from 100% to 77% at around 650 ℃, which can be attributed to the oxidation of carbon in air. This result indicates that the graphite content is approximately 23% in the composite. According to the XPS analysis (SiO_2 weight ratio of approximately 2.0%), the content of SnO_2, SiO_2, and graphite in the SnO_2@SiO_2/G composite is about 75%, 2%, and 23%, respectively.

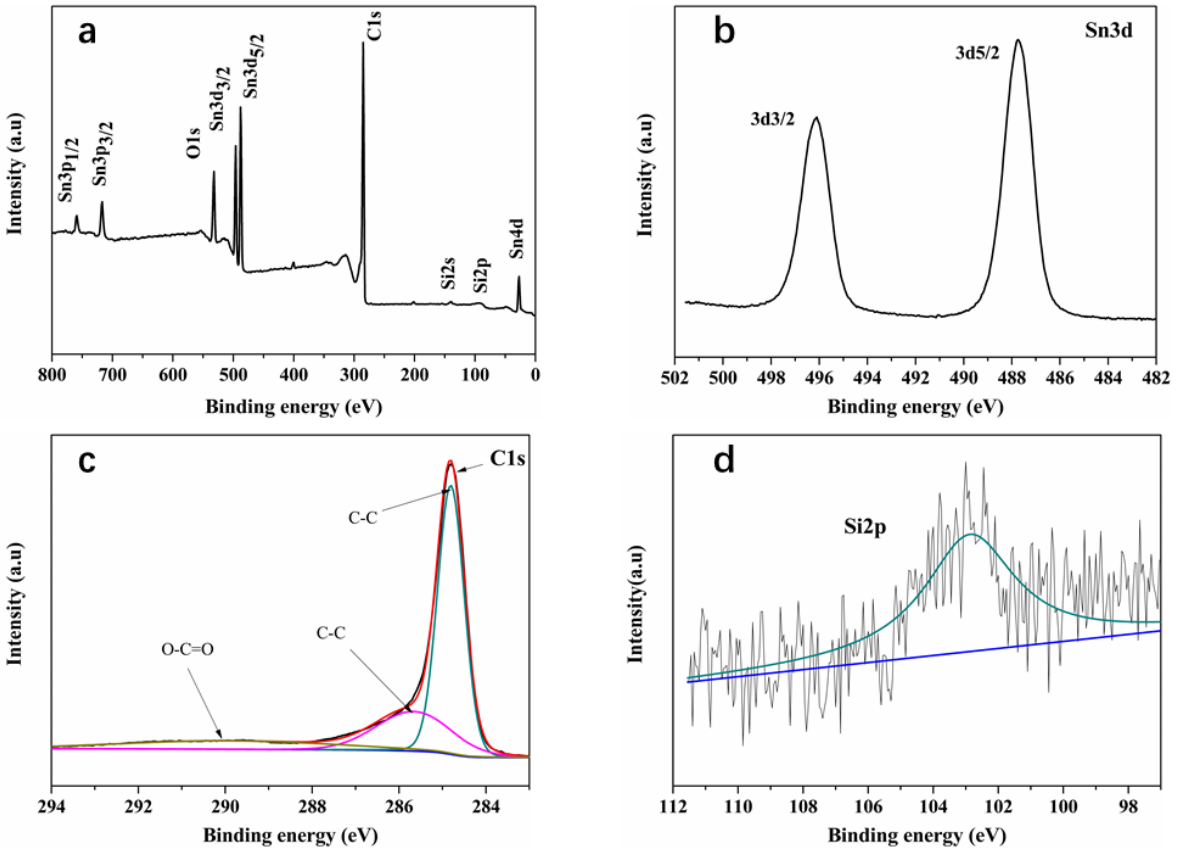

Figure 2. (a) XPS survey spectrum of SnO_2@SiO_2/G. Single elemental spectrum of SnO_2@SiO_2/G: (b) Sn 3d, (c) C 1s, and (d) Si 2p.

The structure of the SnO_2@SiO_2/G composite was further studied using Raman spectroscopy, as shown in Fig. 1(c). Two weak peaks can be observed at 283 and 466 cm^{-1}, corresponding to the Si-O-Si bending and stretching vibrations and E_g vibration mode of SnO_2, respectively [20, 21], which are attributed to the nanosize and coating of the graphite sheets [22]. The two obvious peaks in Fig. 1(d) at around 1360 and 1590 cm^{-1} are ascribed to the D-band and G-band of carbon, respectively. The D peak reflects the defect in the lattice of the carbon atom, which may be attributed to the peeling of graphite

during milling with the SnO2@SiO_2 mixture, while the G peak represents the in-plane stretching vibration of the sp^2 hybrid of the carbon atom, which is a first-order Raman scattering process [22, 23]. In addition, the peak at around 2710 cm^{-1}, corresponding to the 2D band of graphite, is the second order of the D peak caused by the double resonant Raman scattering with two-phonon emissions. This light blue shift, relative to the standard value at 2700 cm^{-1} of pure graphene, confirms that the milled graphite becomes thinner after milling with the SnO_2@SiO_2 mixture [24].

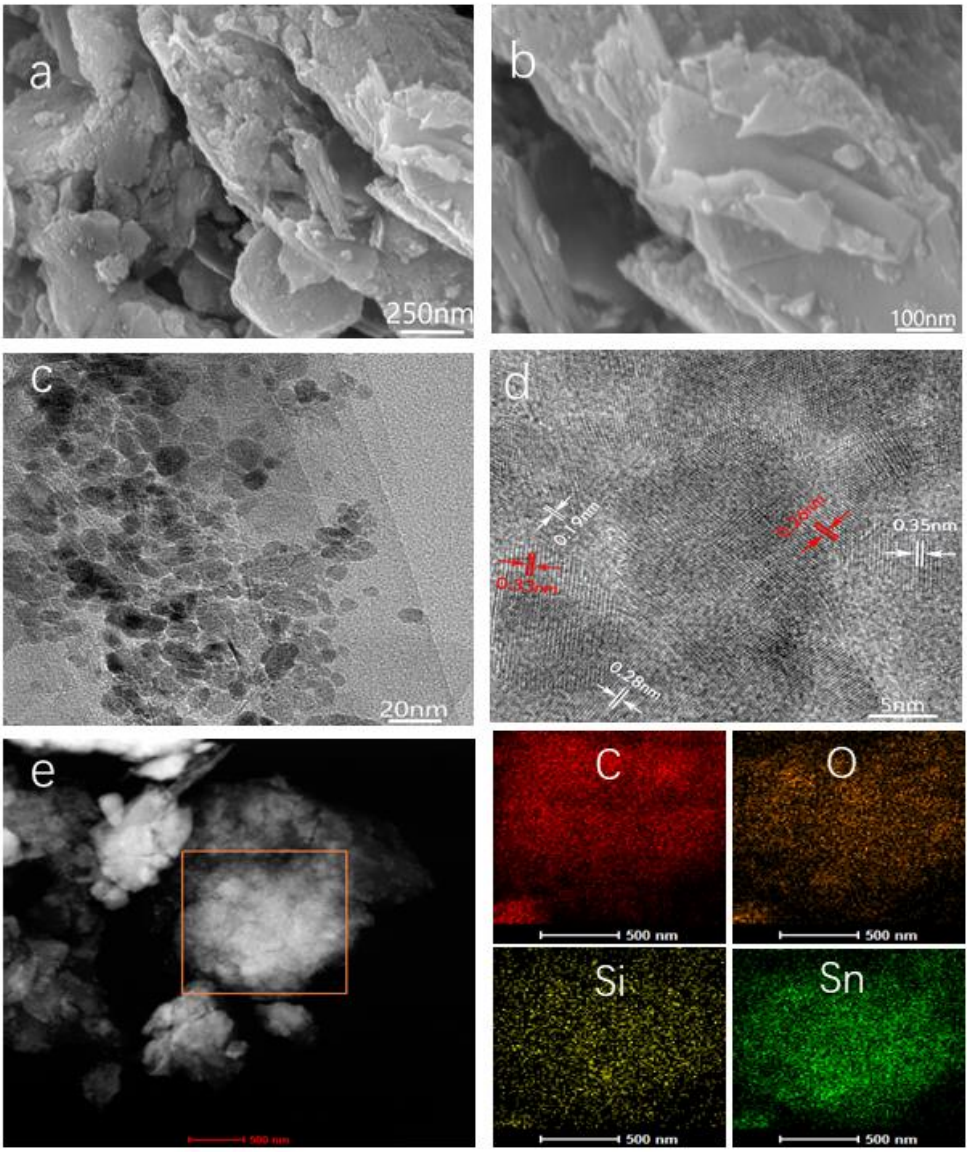

Figure 3. Microstructures and morphology of the SnO_2@SiO_2/G composite: (a, b) SEM image, (c) TEM micrograph, (d) HR-TEM micrograph, (e) elemental mapping images (left image shows the selected area, and images on the right display the elemental mapping of the selected area).

XPS was performed to determine the valence state and elemental composition of the SnO_2@SiO_2 /G composite, and the results are displayed in Fig. 2. The XPS survey spectrum in Fig 2(a) shows that Si, Sn, O, and C are present in the SnO_2@SiO_2/G composite. The high-resolution XPS spectrum of Sn 3d is shown in Fig 2(b). The two peaks at 496.2 eV ($3d_{3/2}$) and 487.8 eV ($3d_{5/2}$) represent the spin-orbit

peaks of SnO_2 in the 3d spectrum of Sn, indicating the existence of Sn^{4+} and formation of SnO_2 [25]. The high-resolution XPS spectra of C 1s, as shown in Fig 2(c), has two peaks found at around 284.7 (285.8) and 289.2 eV, which correspond to the C–C and O–C=O bonds, respectively[26, 27]. Finally, the peak at 103 eV in the Si 2p XPS spectra, as shown in Fig. 2(d), demonstrates the formation of SiO_2[28].

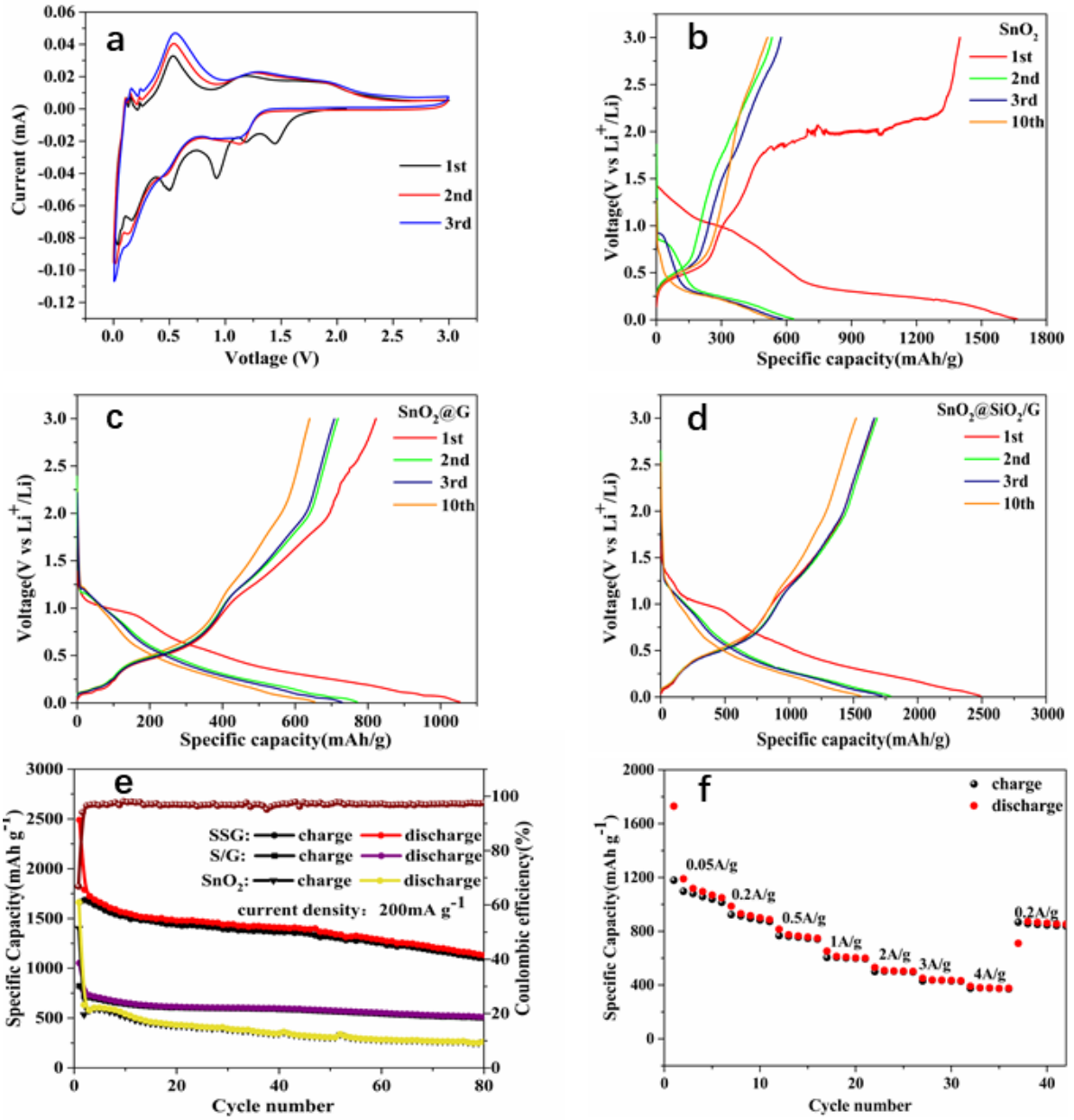

Figure 4. (a) CV curves of the SnO_2@SiO_2/G electrode at a scan rate of 0.1 mV s^{-1}. Galvanostatic discharge–charge profiles of the first three and tenth cycles for (b) SnO_2, (c) SnO_2@G, and (d)SnO_2@SiO_2/G. (e) Cycle performances of SnO_2, SnO_2@G (S/G) and SnO_2@SiO_2/G (SSG) at a current of 200 mA g^{-1}. (f) Rate performance of SnO_2@SiO_2/G.

The morphology and microstructures of the SnO_2@SiO_2/G composite were investigated using SEM and TEM at different magnifications, and the results are shown in Fig. 3(a) to (d). As shown in the micrograph in Fig. 3(a), the synthesized sample exhibits a sheet-like structure with some nanoparticles

adhering thereon. This is more clearly observed in Fig. 3(b), indicating that the SnO_2 and SiO_2 nanoparticles have been successfully incorporated into the graphite sheet, and those that were peeled off during the milling process are also adhered onto the sheet. The sheet-like structure significantly enhances the surface activity of the material, and graphite promotes its ability to conduct electricity.

The nanoparticles can be observed conspicuously in Fig. 3(c). Their size is about 10–20 nm, suggesting the formation of SnO_2 in the hydrothermal process. The sheet-like structure observed in the image improves the tolerance of the composite against the volume expansion of the negative material. Fig. 3(d) shows the high-resolution TEM image of the SnO_2@SiO_2/G composite with markings corresponding to the lattice spacings of 0.33, 0.26, 0.19, 0.28, and 0.35 nm; the first two are attributed to the (110) and (101) crystal planes of SnO_2, respectively, while the final three are ascribed to the (113), (102), and (110) crystal planes of SiO_2, respectively, which are identical to those found in the SiO_2 phase (JCPDS File Card No. 76-0934). The elemental mapping of the sample is shown in Fig. 3(e). The results reveal that Sn, Si, O, and C are distributed uniformly in the as-prepared mixture, signifying that the SnO_2 and SiO_2 nanoparticles are homogenously embedded in the graphite nanosheets.

The CV curves of the SnO_2@SiO_2/G electrode at a scan rate of 0.1 mV s^{-1} and a potential range of 0.01 to 3 V are shown in Fig. 4(a). The following five equations related to the reaction of the CV curves are given to characterise the electrochemical reaction in the charge/discharge process [21, 29].

$$SnO_2 + 4Li^+ + 4e^- \rightarrow 2Li_2O + Sn \quad (1)$$

$$Sn + xLi^+ + xe^- \leftrightarrow 2Li_xSn \quad (2)$$

$$SiO_2 + 4Li^+ + 4e^- \rightarrow 2Li_2O + Si \quad (3.1)$$

$$2SiO_2 + 4Li^+ + 4e^- \rightarrow Li_4SiO_4 + Si \quad (3.2)$$

$$Si + xLi^+ + xe^- \leftrightarrow Li_xSi \quad (4)$$

In the cathodic scan in Fig. 4(a), there are five major cathodic peaks located at approximately 0.125, 0.5, 0.9, 1.12, and 1.5 V. The first peak is ascribed to the alloy reaction of Sn and Si with Li, corresponding to Eq. (2) and (4). The second and fourth peaks originate from the formation of Li-C alloys [25]. The third and fifth peaks correspond to Eq. (1) and (3), respectively, and it can be concluded that the solid electrolyte interface (SEI) appears on the surface of the materials [23]. Meanwhile, SnO_2 and SiO_2 are reduced to elemental Sn and Si with the emergence of the by-product Li_2O [30]. SiO_2 also reacts with Li to form Li_4SiO_4 and Si, resulting in an irreversible capacity and a decrease in capacity during Li insertion and extraction. In the anodic scan, three broad anodic peaks can be observed at 0.6−0.7, 1.25 and 1.9 V. The first peak corresponds to the dealloying reaction of Li_xSn and Li_xSi, while the other two are described by Eq. (1) and (3.1), in which the Sn/Li_2O and Si/Li_2O partly form from SnO_2 and SiO_2, respectively.

The galvanostatic discharge–charge profiles of SnO_2, SnO_2@G, and SnO_2@SiO_2/G at the first, second, third, and tenth cycle at a voltage of 0.01–3 V are shown in Fig. 4(b−d). The comparison in the first charge capacity between SnO_2 and SnO_2@G demonstrates that the addition of graphite significantly improves the charge process because of the large number of active sites in graphite. Furthermore, the addition of SiO_2 promotes the charge specific capacity due to a synergistic effect, as observed from the comparison between SnO_2@G and SnO_2@SiO_2/G. at a current density of 200 mA g^{-1}, the first discharge and charge capacity of the SnO_2@SiO_2/G electrode reach 2489 mA h g^{-1} and 1663 mA h g^{-1}, respectively, corresponding to the reaction of the first cycle of the CV curves. These values are far higher than the

first discharge and charge capacities of SnO_2@G at 1052 mA h g^{-1} and 822 mA h g^{-1}, respectively, and that of SnO_2 at 1663 mA h g^{-1} and 1400 mA h g^{-1}, respectively. The significant enhancement in capacity is mainly ascribed to the formation of SiO_2 during milling, as the microstructure of SiO_2 provides more space for the lithium-ion during the lithiation and delithiation processes. The second discharge capacity of the SnO_2@SiO_2/G electrode is approximately 1750 mA h g^{-1}; the loss is attributed to the emergence of the SEI layer and the unconverted Li_2O [31]. After the tenth cycle, the discharge specific capacity of SnO_2@SiO_2/G decreases to 1557 mA h g^{-1}, and its coulombic efficiency is 97%, which is much better than that of SnO_2@G and SnO_2.

Table 1. Electrochemical performance comparison of SnO_2-based anodes for lithium-ion batteries.

Anode materials	Capacity (mA h g^{-1})	Current density (mA g^{-1})	Cycle number	Refs.
SnO_2 nanowire arrays	510	780	50	[9]
SnO_2@ amorphous-silicon on CNT paper	892	250	25	[10]
SnO_2-graphite nanocomposite	400	200	100	[11]
SnO_2/graphene nanocomposite	1156	100	100	[12]
quantum dots SnO_2/Fe_3O_4 composites	935	100	100	[13]
SnO_2 nanowires on MnO_2 nanosheets	862	100	200	[14]
SnO_2-CuO-graphite composite	561.2	100	150	[15]
Li_2SiO_3@Li_2SnO_3/SnO_2 composite	206.7	150	50	[16]
Sn/SnO_2@graphene composite	695	100	75	[17]
SnO_2@SiO_2/graphite composite	1132	200	80	This work

The cycling performance of the SnO_2@SiO_2/G electrode was investigated, and the results are shown in Fig. 4(e). The reversible capacity of SnO_2@SiO_2/G after 80 cycles at the current density of 200 mA g^{-1} is 1132 mA h g^{-1}, which is more than twice of that of both SnO_2@G and SnO_2. Although the specific capacity of SnO_2@SiO_2/G is declining, it remains to have a better cycle performance than SnO_2@G and SnO_2. In order to clearly demonstrate the superiority of the SnO_2@SiO_2/G composite over similar anode materials, the cycling performance of other previously reported SnO2-based anode materials is listed in Table 1. The table shows that the SnO_2@SiO_2/G composite has a better electrochemical performance than other SnO_2-based anode materials. The outstanding cycling performance of the SnO_2@SiO_2/G composite is attributed to the formation of SiO_2 during milling, which can provide a buffer against volume change in the composite. Moreover, the structure of the SnO_2 and SiO_2 nanoparticles adhered to the graphite sheet further limits the expansion of SnO_2 and promotes the conductivity of the material. Fig. 4(f) shows the rate performance of SnO_2@SiO_2/G at current densities ranging from 0.05 to 4 mA g^{-1} and at 0.2 mA g^{-1}. The rate performance of the SnO_2@SiO_2/G electrode constantly decreases with the increasing current density, but it returns to a corresponding capacity at a current density of 200 mA g^{-1}. The high rate capacity of the composite indicates the rapid diffusion of the Li ions or electrons, which could be due to the graphite nanosheets that anchor the SnO_2 and SiO_2 nanoparticles.

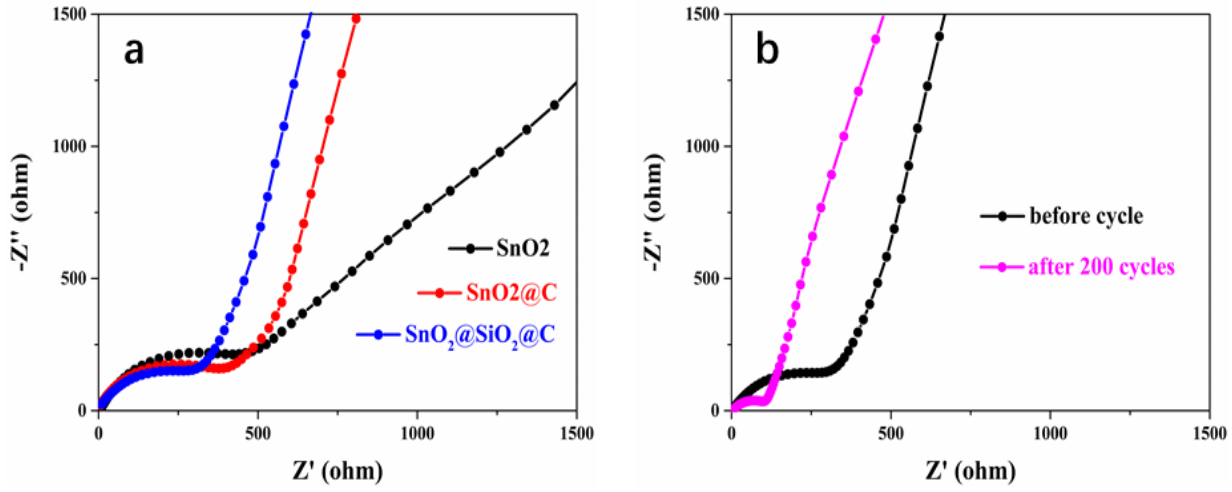

Figure 5. Electrochemical impedance spectra for (a) SnO_2@SiO_2/G, SnO_2@G and SnO_2, (b) SnO_2@SiO_2/G before and after cycling.

Fig. 5 (a) shows the electrochemical impedance spectroscopy (EIS) for the SnO_2@SiO_2/G, SnO_2@G, and SnO_2 electrodes. The curves are composed of two parts: a semicircle and an inclined line. The first part is a semicircle at high frequency, partly derived from the charge transfer resistance. The second part is a sloping line at low frequency, which is attributed to the Li^+ diffusion resistance. The tilt angle of the inclined line suggests that volume expansion occurs during the Li^+ insertion/extraction process[32]. The semicircle in the spectrum of the SnO_2@SiO_2/G electrode is smaller than that of the SnO_2@G and SnO_2 electrodes, implying that charge transmits faster in SnO_2@SiO_2/G than in the other composites, leading to a higher voltage. Furthermore, the slope of the lines in the spectra of SnO_2@G and SnO_2 are steeper than that of SnO_2@SiO_2/G, indicating a larger diffusion capacity and smaller volume expansion in the SnO_2@SiO_2/G electrode, which is identical to the result of the CV analysis. Fig. 5 (b) displays the EIS curves of the SnO_2@SiO_2/G electrode before and after cycling. The semicircle after 200 cycle becomes smaller, signifying the resistance of the SEI layer and the decrease in the mobility of the ions. Moreover, the slightly steeper line after 200 cycles is attributed to the slight volume expansion. These results show that the addition of the SiO_2 nanoparticles and graphite effectively reduces the charge transfer resistance, thereby promoting the diffusion of Li^+ and improving volume expansion.

4. CONCLUSION

A facile hydrothermal method and simple ball milling method were employed to fabricate SnO_2@SiO_2/G composite as anode materials for LIBs, which have a large specific capacity and good cycle stability performance. SnO_2 mixed with graphite were also prepared for performance comparison with the SnO_2@SiO_2/G composite. The results show that the formation of the SiO_2 nanoparticles and graphite enhances the electrochemical performance of the composite, and SnO_2@SiO_2/G allows the rapid diffusion of ions and electrons. The improvement in the performance of the composite is attributed

to the intrinsic structure of SnO_2 and SiO_2 adhered to the graphite sheet, which accommodates volume expansion and promotes conductivity. Therefore, SnO_2@SiO_2/G composites are promising anode materials for LIBs.

ACKNOWLEDGEMENTS
This work was supported by Zhongshan Science and Technology Planning Project of Guangdong Province, China (2019A4008) and the National Natural Science Foundation of China (NSFC) (61875187). Miao He is the author to whom any correspondence should be addressed.

References

1. A.S. Arico, P. Bruce, B. Scrosati, J.M. Tarascon, and W.V. Schalkwijk, *Nat. Mater.,* 4(2005) 148.
2. Y. S. M. K. Kang, J. Bre´Ger, C.P. Grey, G. Ceder, *Science*, 311(2006) 977.
3. X. Xiong, G. Wang, Y. Lin, Y. Wang, X. Ou, F. Zheng, C. Yang, J.H. Wang, and M. Liu, *ACS Nano*, 10(2016) 10953.
4. F. Zheng, C. Yang, X. Xiong, J. Xiong, R. Hu, Y. Chen, and M. Liu, *Angew. Chem. Int. Ed.*, 54(2015) 13058.
5. C. Yang, X. Ou, X. Xiong, F. Zheng, R. Hu, Y. Chen, M. Liu, and K. Huang, *Energy Environ. Sci*, 10(2017) 107.
6. R. Hu, Y. yang, T. Liang, X. Tang, B. Yuan, J. Liu, L. Zhang, L. Yang, and M. Zhu, *Energy Environ. Sci*, 10(2017) 2017.
7. Y. Chen, B. Song, R. M. Chen, L. Lu, and J. Xue, *J. Mater. Chem. A*, 2(2014) 5688.
8. Z. Hu, X. Xu, X. Wang, K. Yu, and C. Liang, *J. Alloys Compd.*, 835(2020) 155446.
9. A. Abnavi, M.S. Faramarzi, A. Abdollahi, R. Ramzani, S. Ghasemi, and Z. Sanaee, *Nanotechnology,* 28(2017) 255404.
10. Y.D. Ko, J.G. Kang, J.G. Park, S. Lee, and D.W. Kim, *Nanotechnology,* 20(2009) 455701.
11. V.M.H. Ng, S. Wu, P. Liu, B. Zhu, L. Yu, C. Wang, H. Huang, Z.J. Xu, Z. Yao, J. Zhou, W. Que, and L.B. Kong, *Electrochim. Acta,* 248(2017) 440.
12. P. Lian, X. Zhu, S. Liang, Z. Li, W. Yang, and H. Wang, *Electrochim. Acta*, 56(2011) 4532.
13. X. Gu, L. Chen, Z. Ju, H. Xu, J. Yang, and Y. Qian, *Adv. Funct. Mater.*, 23(2013) 4049.
14. T.L. Nguyen, J. Hur, and I.T. Kim, *J. Ind. Eng. Chem.*, 72(2019) 504.
15. L. Pan, K.X. Wang, X.D. Zhu, X.M. Xie, and Y.T. Liu, *J. Mater. Chem. A,* 3(2015) 6477.
16. S. Yang, J. Zhang, Q. Wang, J. Miao, C. Zhang, L. Zhao, and Y. Zhang, *Mater. Lett.,* 234(2019) 375.
17. W. Jiang, W. Wang, L. Liu, H. Wang, Z. Xu, F. Li, H. Fu, H. Lv, L. Chen, and Y. Kang, *J. Alloys Compd.*, 779(2019) 856.
18. R. Li, W. Xiao, C. Miao, R. Fang, Z. Wang, and M. Zhang, *Ceram. Int.*, 45(2019) 13530.
19. R. Li, C. Miao, L. Yu, M. Zhang, and W. Xiao, *Mater. Lett.*, 272(2020) 127851.
20. F.M. Hassan, V. Chabot, A.R. Elsayed, X. Xiao, and Z. Chen, *Nano Lett.*, 14(2013) 277.
21. D. Wang, X. Li, J. Wang, J. Yang, D. Geng, R. Li, M. Cai, T.K. Sham, and X. Sun, *J. Phys. Chem. C*, 116(2012) 22149.
22. R. Hu, Y. Ouyang, T. Liang, H. Wang, J. Liu, J. Chen, C. Yang, L. Yang, and M. Zhu, *Adv. Mater.*, 29(2017) 1605006.
23. X. Xu, H. Zhang, Y. Chen, N. Li, Y. Li, and L. Liu, *J. Alloys Compd.,* 677(2016) 237.
24. H.W.N.B. Lu, R. Hu. N, Li. Yang, J. Liu, J. Liu, M. Zhu, *Mater. Lett.,*, 185(2016) 9.
25. Y. Zou, X. Zhou, J. Xie, Q. Liao, B. Huang, and J. Yang, *J. Mater. Chem. A*, 2(2014) 4524.

26. D. Chen, X. Chen, H. Gao, and J. Zhong, *RSC Adv.*, 8(2018) 29855.
27. Z. Luo, Y. Li, F. Wang, and R. Hong, *Materials*, 12(2019) 707.
28. S. Sim, P. Oh, S. Park, and J. Cho, *Adv. Mater.*, 25(2013) 4498.
29. B. Guo, J. Shu, Z. Wang, H. Yang, L. Shi, Y. Liu, and L. Chen, *Electrochem. Commun.*, 10(2008) 1876.
30. G. Liang, X. Sun, J. Lai, C. Wei, Y. Huang, and H. Hu, *J. Electroanal. Chem*, 853(2019) 113401.
31. V. Aravindan, J. Sundaramurthy, E.N. Kumar, P.S. Kumar, W.C. Ling, R.V. Hagen, S. Mathur, S. Ramakrishna, and S. Madhavi, *Electrochim. Acta*, 121(2014) 109.
32. X. Liu, Y. Han, J. Zeng, H. Yang, K. Zhou, and D. Pan, *J. Mater. Sci. - Mater. Electron.*, 29(2018) 5710.